Design and Implementation of Quart-Torus Waveguide Filters for Layout Optimization Using Additive Manufacturing Techniques

Alejandro Pons-Abenza, Alejandro Álvarez-Melcón, *Senior Member, IEEE*, Fernando Daniel Quesada-Pereira, *Member, IEEE*, Antonio Romera-Pérez, and Lara Arche-Andradas

***Abstract*— In this contribution, a novel quart-torus cavity for the design of waveguide filters is presented. A filter breadboard based on this kind of cavity is designed at Ku-band, and then fabricated using additive manufacturing (AM) techniques. The objective is to optimize the footprint distribution of cavity filter structures without compromising their electrical performance. The proposed resonator is built by applying a circular revolution process to a 2-D surface generator. The presented study is performed for circular and elliptical cross-sectional quart-torus cavities. The resonances found in the proposed cavities show similar theoretical unloaded-Q factors (Q_U) to their equivalent circular waveguide cavities (around $Q_U = 5000$), while exhibiting interesting advantages in terms of physical layout disposition, due to the bending applied. To demonstrate the feasibility of the proposed idea, a tenth-order in-line bandpass filter is designed with elliptical quart-torus (EQT) cavities. Due to the geometrical complexity, a prototype is manufactured using a selective laser melting (SLM) technique, and its measured response has shown very good agreement with respect to the full-wave simulations from the ideal designs. Measured results show a fractional bandwidth (FBW) of 5.3%, with return losses (RLs) better than 20 dB, and unloaded quality factor (Q_U) above 700. The footprint optimization and flexibility offered by the new concept can make these AM filters a very attractive option for the microwave industry.**

Manuscript received 4 April 2023; revised 15 June 2023 and 4 July 2023; accepted 7 July 2023. This work was supported in part by Thales Alenia Space, Tres Cantos, Madrid, Spain, through the Project "Diseño e Implementación de Nuevas Estructuras de Filtros de Microondas Usando la Técnica de Fabricación Aditiva"; in part by the Spanish Ministerio de Ciencia e Innovación through the Frame of the Cooperative Project "Green and Efficient Technologies for Advanced Telecommunication Systems (GRETAS)" with Reference TPID2019-103982RB-C42 under Grant MCIN/AEI/10.13039/501100011033; in part by the Agencia Estatal de Investigación, European Union Next Generation Funds, through the Project "Antennas and Circuits for Efficient Wireless Sensor Networks Using Low-orbit Satellites (ARIELS)," with Reference TED2021-129196B-C42; and in part by Fundación Séneca, Agencia de Ciencia y Tecnología de la Región de Murcia, Spain, which is included in the Regional Program for the Promotion of the Research (2022), "Componentes Radiantes y de Filtrado de Microondas Para Satélites Emergentes," under Project 22076/PI/22. *(Corresponding author: Fernando Daniel Quesada-Pereira.)*

Alejandro Pons-Abenza, Alejandro Álvarez-Melcón, Fernando Daniel Quesada-Pereira, and Antonio Romera-Pérez are with the Department of Information and Communication Technologies, Universidad Politécnica de Cartagena, 30202 Cartagena, Spain (e-mail: fernando.quesada@upct.es).

Lara Arche-Andradas is with Thales Alenia Space, Tres Cantos, 28760 Madrid, Spain.

Color versions of one or more figures in this article are available at https://doi.org/10.1109/TMTT.2023.3297717.

Digital Object Identifier 10.1109/TMTT.2023.3297717

***Index Terms*— Additive manufacturing (AM), quart-torus cavities, 3-D printing, waveguide filters.**

I. Introduction

THE design of microwave filters for satellite communications in waveguide technology is an interesting subject of research in the scientific community. Because of its inherent physical dimensions, waveguide technology is "bulkier" than other typical planar technologies (e.g., substrate-integrated waveguide (SIW) and microstrip components). On the other hand, waveguides show interesting electrical properties, such as low-loss and high-power-handling capability, thus making them very attractive for communication satellite payloads (specially at the input–output (I/O) stages, respectively). However, the standard waveguide filter geometries typically used in space applications are limited by traditional milling manufacturing techniques, which are well known and can be found in many papers and textbooks, such as [1] and [2]. As a consequence, the performance of these filters is bounded by the rigid geometrical parameters of the standard cavity resonators and by the design parameters of the filtering functions.

In recent years, additive manufacturing (AM) processes have attracted a lot of attention to the aerospace industry sector [3]. From the RF-field perspective, AM has extensively been tested to replace traditional implementations of microwave components. In particular, the waveguide technology can be mostly benefited from these manufacturing techniques. Several research works can be found where the pure waveguide section is manufactured using different conductor materials, such as aluminum and titanium alloys or copper-metallized plastics, within various frequency ranges [4], [5], [6], [7], [8], [9], with promising results in terms of mass reduction and electrical performance. On the other hand, availability of materials and surface roughness of the final manufactured parts are two critical factors that limit their usage in real space applications [10], [11], [12], since they have strong negative impact on unloaded quality factors (Q_U). Still, around 80% of the expected Q_U can be recovered if chemical polishing and silver plating operations are applied to the 3-D manufactured surfaces [13].

In this context, AM techniques are specially useful if complex geometries are introduced to conceive novel waveguide

devices. In fact, AM processes allow the implementation of very complex geometries, which is a useful capability that may help to overcome previous geometrical limitations, and can be employed to optimize the filter performance. These manufacturing techniques provide many interesting features from the mechanical and electrical points of view. As compared with traditional milling techniques, the geometries for additive manufactured parts are more flexible and admit structures in just one block, due to their layer-by-layer building strategy. Therefore, screws for housing and top cover assemblies are no longer required. In addition, geometry optimization of the resonant cavities can improve the electrical performance of the whole filter. These improvements are obtained in the form of better theoretical Q_U, wider spurious-free range (SFR), or higher compactness. The design and optimization of 3-D geometries are already under study, and many works can nowadays be found in the scientific literature. For instance, smart optimization of traditional implementations allows to improve the theoretical Q_U of the filter [13]. Direct geometrical modifications on the cavity resonator, using curvilinear shapes, have led to new resonators with significant improvements in terms of theoretical Q_U [14]. All these improvements cannot be obtained simultaneously, and a trade-off depending on the required application must usually be adopted.

One possible objective for space communication systems is to obtain improvements in terms of mass, volume, and footprint, in contrast with standard canonical implementations. For instance, due to the limited footprint available in many of these applications, the RF components should be carefully designed to optimize the physical layout disposition. One idea, that we explore in this article, is to use complex geometries in combination with AM techniques, to optimize the footprint distribution along the available surface in the spacecraft.

To address this issue, in this work, a resonator based on a circular cylindrical cavity is studied. These cylindrical cavities are traditionally employed for dual-mode operation using $\mathrm{TE}_{11\rho}$ modes. The cavity is not employed as a single-mode resonator because of its significant dimensions, even though high Q_U factors are achieved as compared with rectangular cavity resonators. The strategy that we propose to increase flexibility in the use of the available footprint on the satellite communication board is to apply a bending along the longitudinal axis, i.e., transforming the cylinder into a circular bend, following the profile of a circular arc instead of a straight line, as shown in Fig. 1. By doing this operation, similar Q_U factors to the standard circular $\mathrm{TE}_{11\rho}$ resonator are obtained, while reducing the total length of the resulting device as compared with traditional in-line cavity-coupled filters. The new circular cylinder-bent cavity will be referred to as a quart-torus cavity and exhibits a theoretical Q_U around (4475 for an isolated cavity tuned at 14.12 GHz with pure aluminum walls). The study of the quart-torus cavity as a microwave resonator is addressed in Section II.

In this study, the resulting quart-torus cavities are operating in single mode. Because of the similarities between the novel proposed cavity and the classical circular cylindrical cavity, it is expected that the "pseudo-degenerated" modes of the new cavity behave similar to the degenerated TE_{111} modes of the

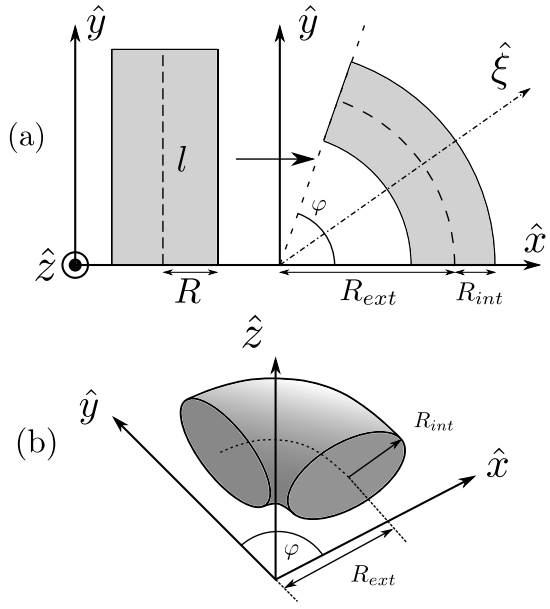

Fig. 1. Construction of the torus geometry. (a) Circular cylinder (left) and the torus geometry obtained by bending the longitudinal axis of the original cylinder (right). Variables R_{ext}, R_{int}, and φ are design parameters for the new cavity. An auxiliary ξ-axis is defined, contained in the XY plane, which will be useful for analysis purposes. (b) 3-D view example of a quart-torus geometry, generated with $\varphi = 90°$.

circular cavity. This would allow a further reduction in terms of footprint, leading to even more compact filter structures. However, due to the introduced curvatures, there are also some important challenges to overcome, before a final prototype with dual-mode quart-torus cavities is manufactured.

A similar family of filters can be found in the technical literature. Structures based on connecting 90° E-plane bends to produce bandpass filters are explored in [15] and [16]. These "meandered" waveguide filters are designed using the classical stepped impedance synthesis, in the context of high-pass–low-pass filters to generate bandpass responses. The geometry of each bend is designed to implement the corresponding values of the characteristic impedance Z_i required for each step of the filter. In this article, we approach the "bending" of the waveguides in a different way, using the bent circular and elliptical waveguides as coupled resonant cavities. For this reason, the coupling matrix formalism is employed in the design of these quart-torus filters. In this sense, the proposed cavity-coupled family of filters is a novel solution taking advantage of AM techniques, illustrating the potential of these novel manufacturing methods to further enhance the performance of milled waveguide filters. However, the footprint optimization strategy followed is similar to the meandered waveguide structures [15], [16].

To validate the proposed cavity for the design of microwave filters, a tenth-order Ku-band in-line filter is designed and manufactured. In order to avoid spurious resonances of the original cavity, the circular shape of the surface generator is further transformed into an ellipse. A similar strategy is followed in other AM works, such as [14] and [17], by "squeezing" the cavity geometry to suppress a spurious mode of the resonator. It is demonstrated that, with the elliptic shape, the

operational mode is substantially separated in frequency from other spurious resonances. The elliptical refinement of the quart-torus cavity is discussed in Section III-A.

The physical implementation of the designed filter is carried out in a single piece, thus avoiding the typical requirement of splitting the filter structure into several pieces. This feature completely removes the need to account for assembling screws. The whole structure is directly manufactured using a single-part metallic body; thus, a selective laser melting (SLM) [18] process is adequate for this task. The design process of a tenth-order elliptical quart-torus (EQT) cavity filter is addressed in Section III-B, while the measured results are presented in Section IV.

II. Quart Torus as a Microwave Resonator

The proposed geometry for the cavity resonator is based on the classical circular waveguide geometry. This structure is mainly employed in the design of cross-coupled topologies with real or complex transmission zeros (TZs), due to the inherent capability of the circular waveguide TE_{11} fundamental mode to become degenerated. This degeneration is possible due to the cavity being completely symmetrical along the cylinder cross section ($\hat{x}$- and $\hat{z}$-axes) shown in Fig. 1(a) [1]. In this section, an in-depth study of the resonances inside the torus-based cavity is presented. First, a characterization of the modes in terms of their electric-field vector distribution and modal charts is presented. Then, a second study is carried out introducing the elliptical torus cavity, as an interesting solution to operate the proposed geometry as a single-mode resonator.

A. Modal Characterization of the Circular Torus Cavity

The new proposed cavity, as it is shown in Fig. 1(a) (right), is generated by the revolution of a circle with radius R_{int} (alternatively, it can also be seen as a bending of the circular cylindrical waveguide along the longitudinal $\hat{y}$-axis). The generator surface is placed at a distance R_{ext} from the revolution axis, in order to extrude the circle along a circular arc with radius R_{ext} and revolution angle φ. By performing this revolution operation, the cavity 3-D volume can be obtained. The 2-D schematic illustrating the proposed structure parametrization is presented in Fig. 1(a). A 3-D view of the resulting volume is illustrated in Fig. 1(b), as an example, with $\varphi = 90°$.

The following study is performed with the objective to obtain the optimal dimensions of the resulting resonator to operate at Ku-band frequencies. In order to characterize the performance of the cavity as a microwave resonator, the first step is to study how its modal chart changes when the revolution angle φ is modified. For this purpose, the other dimensions are fixed to $R_{\text{int}} = 9$ mm and $R_{\text{ext}} = 10$ mm, and the sweep for the revolution angle is performed in the range $30° < \varphi < 150°$. No smaller values than $\varphi = 30°$ have been considered, due to the expected Q_U reductions and manufacturing difficulties. In addition, the upper bound $\varphi = 150°$ analysis has been chosen to avoid higher order resonances near the fundamental mode. A modal chart as a function of φ is presented in Fig. 2, showing the first five resonant modes.

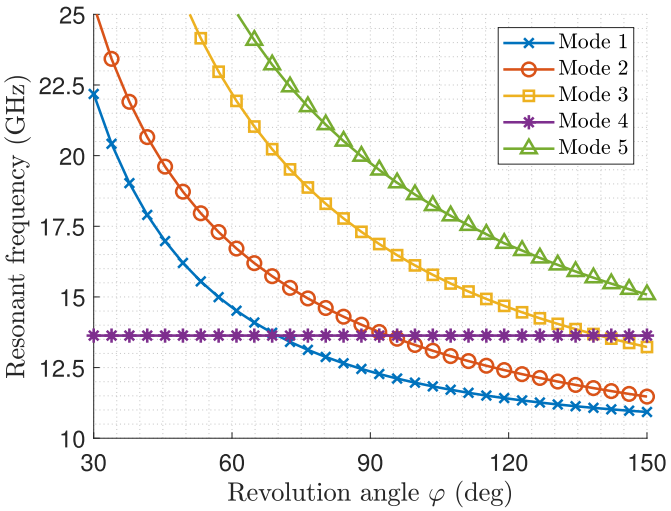

Fig. 2. Modal chart as a function of the revolution angle φ, using a circular quart-torus cavity with fixed $R_{\text{int}} = 9$ mm and $R_{\text{ext}} = 10$ mm. Presented modes have been sorted according to the modal distribution at $\varphi = 150°$.

Similarities between the resonant modes present in this structure, and those corresponding to the classical circular cylindrical cavity can be observed. For instance, mode 4 from the chart in Fig. 2 shows an invariant behavior with φ. This is similar to the TM_{010} mode from the circular cylindrical cavity, which shows no frequency variation with the cylinder length. On the other hand, degenerated modes TE_{111} from the circular cylindrical cavity are very similar to modes 1 and 2 from the chart in Fig. 2. In this case, these modes are not degenerated because of the curvature introduced in the geometry. This curvature breaks the structure symmetry, and thus, these modes no longer resonate at exactly the same frequency. It is interesting, though, to see how these modes become pseudo-degenerated again at $\varphi \approx 150°$.

From the design point of view, it is convenient to identify the nature of these modes. For this purpose, the electric-field lines distribution is plotted for the central XY cut plane (at a half of the total distance along the $\hat{z}$-axis). The electric-field lines corresponding to modes 1 and 2, which are shown in Figs. 3 and 4, can confirm that these are TE quasi-degenerated modes. It can be noted that the maximum electric field for the modes is located in the geometrical center of the cavity. For this reason, an auxiliary axis $\hat{\xi}$ is defined, by shifting 45° the $\hat{x}$-axis. Using this auxiliary axis, the field lines on the ξZ plane can be properly plotted. Thus, for the sake of completeness, in Fig. 5, the electric-field lines corresponding to mode 2 are shown, illustrating the ξZ electric-field components, for a central ξZ cut plane with $\varphi = 45°$ (see Fig. 1). For mode 2, the electric-field predominant component is directed toward the $\hat{z}$-axis, while the predominant component for mode 1 is directed toward the ξ-axis, as it is shown in Fig. 3. In fact, the electric-field lines are orthogonal between them, and they tend to be transversal to the bending axis. As explained above, their resonant frequencies are not exactly equal because of the asymmetry introduced by the bending.

To confirm that mode 4 of the chart shown in Fig. 2 corresponds to a TM mode, its electric-field distribution is presented in Fig. 6. A strong component of the electric field

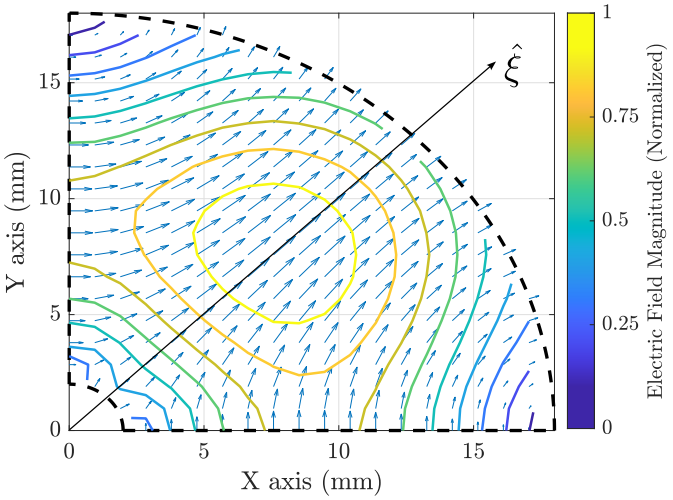

Fig. 3. Normalized electric-field lines distribution corresponding to mode 1 from Fig. 2. Arrow lines correspond to the $\hat{x}$ and $\hat{y}$ components of the electric field, at a $Z = 0$ cut plane (central cut plane to the quart-torus cavity). Level curves correspond to constant electric-field magnitude, computed taking into account all its components (E_x, E_y, and E_z).

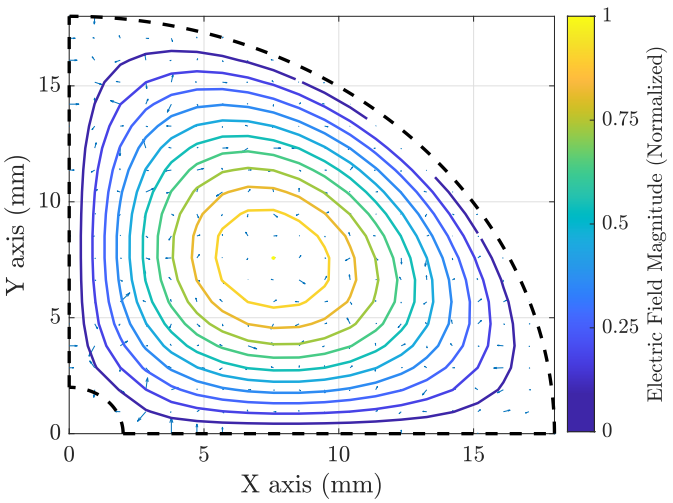

Fig. 4. Normalized electric-field lines distribution corresponding to mode 2 from Fig. 2. Arrow lines correspond to the $\hat{x}$ and $\hat{y}$ components of the electric field, at a $Z = 0$ cut plane (central cut plane to the quart-torus cavity). Level curves correspond to constant electric-field magnitude, computed taking into account all its components (E_x, E_y, and E_z).

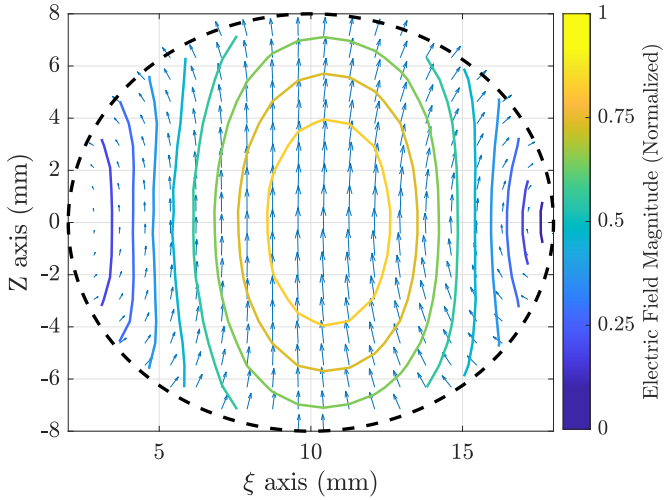

Fig. 5. Normalized electric-field lines distribution corresponding to mode 2 from Fig. 2. Arrow lines correspond to the ξ and $\hat{z}$ components of the electric field, for the ξ-axis placed at $\varphi = 45°$. Level curves correspond to constant electric-field magnitude, computed taking into account all its components (E_x, E_y, and E_z).

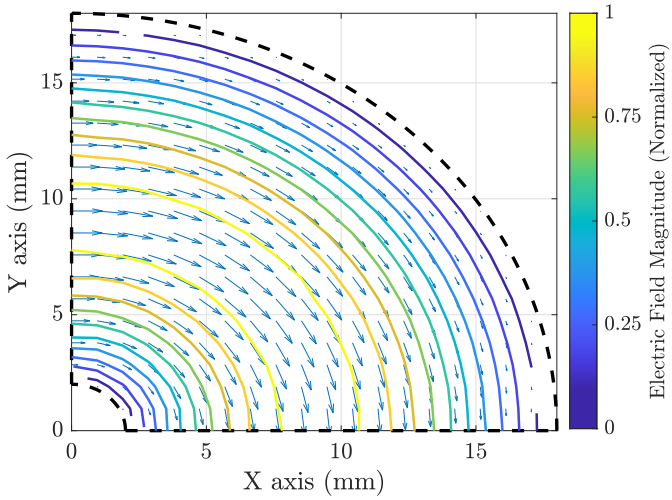

Fig. 6. Normalized electric-field lines distribution corresponding to mode 4 from Fig. 2. Arrow lines correspond to the $\hat{x}$ and $\hat{y}$ components of the electric field, at a $Z = 0$ cut plane (central cut plane to the quart-torus cavity). Level curves correspond to constant electric-field magnitude, computed taking into account all its components (E_x, E_y, and E_z).

along the bending axis is observed, thus implying that the magnetic field is minimum or close to zero. This confirms its TM nature. For reasons that will be evident in Section II-B, we will operate this cavity with mode 2 shown in Fig. 4.

It is important to note that, for a fixed resonant frequency, there could be several combinations of the torus radii R_{ext}, R_{int}, and φ angle that achieve the desired frequency. Selecting one combination over the other will heavily depend on the application of the filter to be designed. An appropriate way to proceed when designing these resonators is to fix the resonant frequency f_0 and one of the radii to our convenience (for simplicity, it is better to fix R_{ext}). Afterward, a similar analysis should be performed but obtaining a curve with several cavities tuned at f_0 as a function of φ and the other radius (R_{int}). With this information, we can evaluate their electrical performance, in particular, the unloaded-Q factors, spurious resonances, volume, footprint, and so on. This information allows to choose the most adequate cavity dimensions for the required application.

For this purpose, a second study is carried out, considering the effects of R_{ext} and R_{int} in the electrical behavior of the resonator.

Intuitively, both R_{ext} and R_{int} parameters will affect to the resonant frequency, as well as to the final Q_U. For the sake of simplicity, an additional parameter is now defined, namely, the cavity aspect ratio (AR), as follows:

$$\text{AR} = \frac{R_{\text{int}}}{R_{\text{ext}}} \tag{1}$$

where $R_{\text{int}} \leq R_{\text{ext}}$, with the objective to avoid geometry distortions. As a consequence, the range of possible geometries will be defined between $0 < \text{AR} \leq 1$. Taking as initial

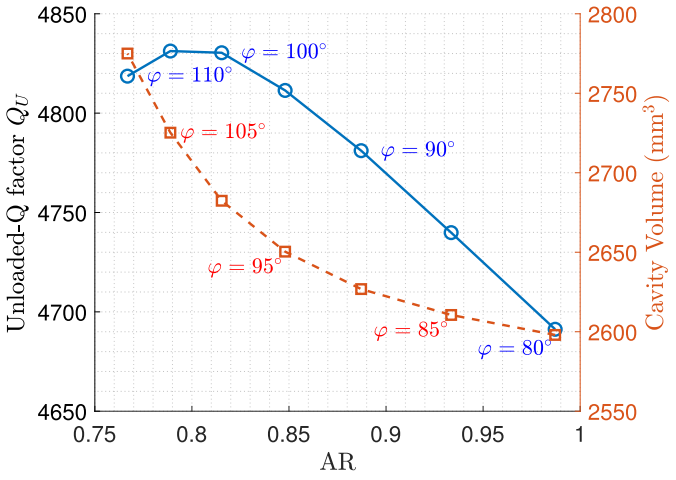

Fig. 7. Q_U curve (blue) as a function of AR, computed for relevant values of the revolution angle φ. The parameter R_{int} is adjusted to keep the same resonant frequency at 14.12 GHz for all five cavities, while R_{ext} is fixed to 10 mm. The corresponding cavity volume is also presented in the red curve. The analysis is performed using resonant mode 2 from the previous study.

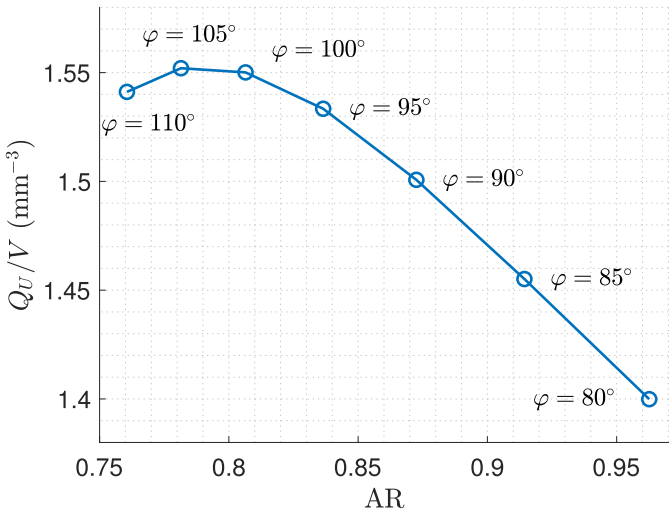

Fig. 8. Q_U/V curve as a function of φ, adjusting the AR to keep the same resonant frequency at 14.12 GHz for all seven cavities. The AR is obtained by adjusting the parameter R_{int}, while R_{ext} is fixed to 10 mm. The analysis is performed using resonant mode 2 from the previous study.

dimensions a quart-torus cavity with a resonant frequency of 14.12 GHz, it is possible to obtain a set of geometries with different ARs. In this study, the value of AR is adjusted to keep the same resonant frequency for the operating mode (mode 2 from the previous study), for different values of the revolution angle φ. With a fixed resonant frequency, the study can now be focused on the electrical performance of this set of resonators. To evaluate their behavior, two parameters are considered: first, the cavity volume, which is calculated by means of analytical formulas, and, second, the Q_U, computed using the full-wave simulator Ansys High-Frequency Structure Simulator (HFSS) [19]. For a fair comparison, all resonators are now simulated using the conductivity of the aluminum alloy employed in the manufactured prototype (AlSi10Mg), as a finite conductivity boundary condition in the walls, with a conductivity $\sigma = 1.7 \times 10^7$ S/m.

In Fig. 7, the Q_U is represented as a function of AR, as well as the volumes corresponding to those cavities. The volume of a torus cavity sector is analytically calculated by means of the centroid Pappus theorem, as follows:

$$V = \pi \varphi R_{\text{ext}} R_{\text{int}}^2. \tag{2}$$

Seven cavities are studied for relevant values of the revolution angle φ. The AR is modified by adjusting R_{int} while fixing $R_{\text{ext}} = 10$ mm. According to the results shown, the maximum Q_U is obtained for cavities with larger AR, which also correspond to smaller values of φ. The volume of these seven cavities is also compared in Fig. 7, verifying that maximum Q_U is achieved for the most voluminous cavities.

It would be interesting to obtain the cavity that exhibits not only the best Q_U, but also the most reduced physical size. One possibility is to define another figure of merit, namely, the ratio between Q_U and cavity volume, as shown in Fig. 8. In this case, the curve represents the Q_U/V ratio, as a function of φ, clearly illustrating that the most efficient cavity, in terms of exploitation of Q_U per unit volume, corresponds to a cavity with $\varphi \approx 105°$.

B. Elliptical Torus Cavity

From the analysis presented in Section II-A in search of the optimal φ cavity in Fig. 8, it is concluded that the optimal circular torus cavity is located around 100° and 105°. However, comparing these results with the modal chart presented in Fig. 2, it can be observed that for the optimal-angle cavity, there exist at least three resonant modes, which are very close in frequency. If these three modes are excited together, it would be difficult to design a cavity filter due to the inter-cavity and inter-resonator couplings, which may be difficult to control.

To overcome this problem, a geometrical refinement is now introduced. First, we inspect the electric-field lines of the three resonant modes under study, which correspond to modes 1, 2, and 4 from Fig. 2. It is easy to observe that the electric-field lines of mode 2 (the desired mode for the prototype filter) have a predominant $\hat{z}$ component, as shown in Fig. 5 (perpendicular to the XY cut plane shown in Fig. 4). On the contrary, the electric-field lines for modes 1 and 4 show the predominant component parallel to the XY cut plane (see Fig. 3 for mode 1 and Fig. 6 for mode 4). This is an interesting property of the relevant resonances, which can be exploited to modify the field distribution in order to separate operating mode 2 from the other two modes.

To proceed, the circular shape of the surface generator in the quart-torus cavity is now replaced by introducing a second degree of freedom. This is done by transforming the circle into an ellipse, as shown in Fig. 9. Now, instead of using only the radius R_{int}, the elliptical semiaxes a_x and a_z will be employed. Intuitively, the modification of the a_z-axis should barely affect to the resonant frequency of mode 2, while it will significantly modify the resonant frequencies of modes 1 and 4.

In order to validate this approach, a new study of the EQT cavity is performed. The idea is to begin with a circular quart-torus cavity, where $a_x = a_z$, and then vary the dimensions of one ellipse axis, fixing the rest of the cavity dimensions. For the sake of simplicity, the results are presented as a

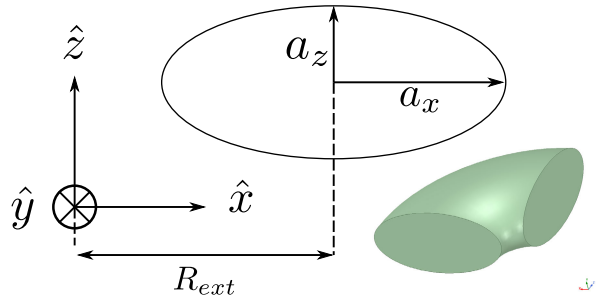

Fig. 9. 2-D parametrization of the elliptic quart-torus resonator.

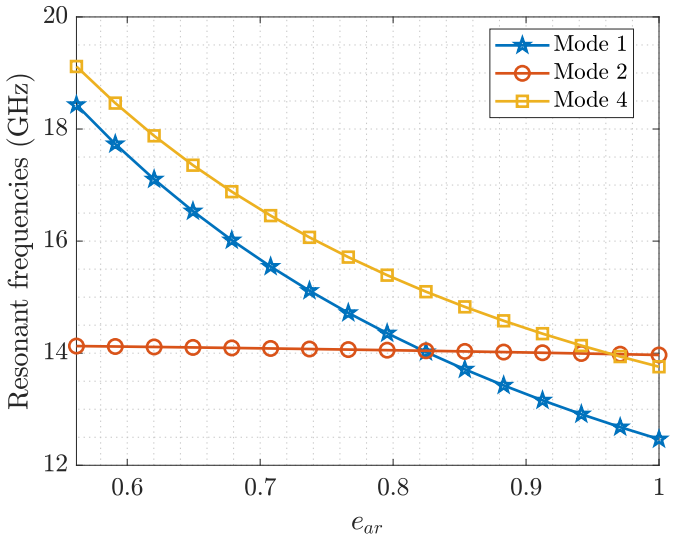

Fig. 10. Modal analysis (resonant frequency) for the ellipse axial ratio E_{ar}, fixing $a_x = 8.9$ mm, $R_{\text{ext}} = 10$ mm, and $\varphi = 90°$. Only the most relevant modes (1, 2, and 4 from Fig. 2) are considered.

function of the ellipse axial ratio $E_{\text{ar}} = a_z/a_x$. The results of the study are shown in Fig. 10, where a parametric sweep for a_z (5 mm $< a_z <$ 8.9 mm), fixing $a_x = 8.9$ mm, $\varphi = 90°$, and $R_{\text{ext}} = 10$ mm, is performed. The dimensions corresponding to a_x and R_{ext} have been fixed to tune the resonant frequency of mode 2 to 14.12 GHz. Remember that the case for $a_{\text{er}} = 1$ corresponds to the original circular quart-torus cavity modal distribution. As expected, mode 2 shows a constant behavior, as E_{ar} is decreased, while the two spurious modes are shifted to higher frequencies. As a consequence of this geometry change, it is expected to obtain slightly lower Q_U factors, due to the volume reduction of the elliptical cavity. This behavior can be observed in the Q_U curves shown in Fig. 11, for the same analysis presented in Fig. 10. Results confirm that the quality factors decrease due to the volume reduction of the elliptical cavity. On the other hand, the range of spurious free resonances considerably increases.

C. Optimal Geometry for the Elliptical Torus Cavity

In this section, a modal study of the elliptical torus cavity is presented. The objective is to determine the best geometries to design a microwave filter using the proposed elliptical cavity. For this purpose, a similar analysis as the one conducted for the circular torus cavity in Section II-A is performed.

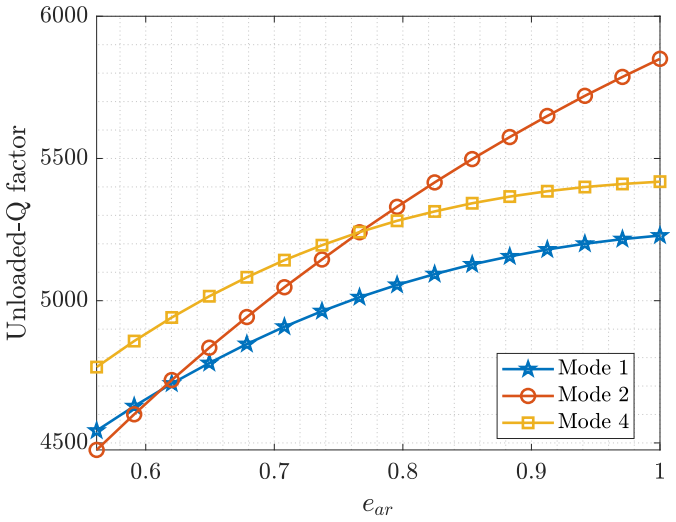

Fig. 11. Unloaded quality factors (Q_U), using AlSi10Mg walls with a conductivity $\sigma = 1.79 \times 10^7$ S/m, as a function of the ellipse axial ratio a_{er}, fixing $a_x = 8.9$ mm, $R_{\text{ext}} = 10$ mm, and $\varphi = 90°$. Only the most relevant modes (1, 2, and 4 from Fig. 2) are considered.

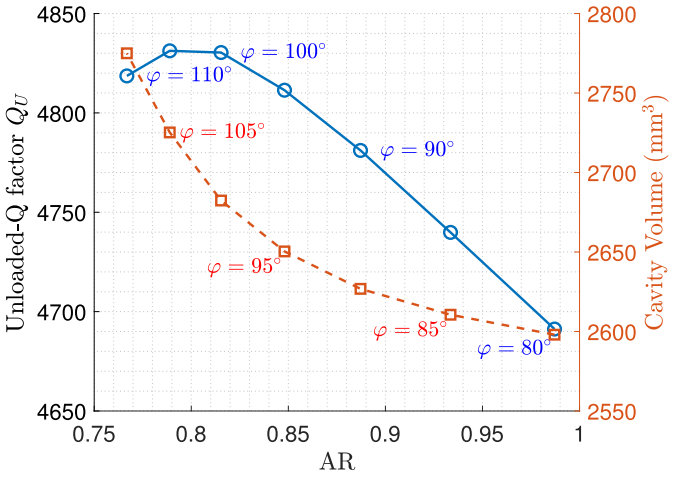

Fig. 12. Q_U and volume corresponding to several cavities with different φ angles, as a function of AR. Fixed dimensions are $R_{\text{ext}} = 10$ mm and $a_z = 6$ mm. Cavities resonate at a fixed $f_0 = 14.12$ GHz.

In contrast with the previous study, there are two radii available to tune the resonant frequency of the elliptical cavity (a_x and a_z). For the sake of simplicity, the radius a_z is fixed to 6 mm, whereas the a_x radius will be analyzed between 7.5 and 9.9 mm in order to produce cavities resonating at $f_0 =$ 14.12 GHz. This geometry sweep is performed for various values of the φ angle. The external radius R_{ext} is also fixed to 10 mm. To compute the unloaded-Q factors, a conductivity of $\sigma = 1.7 \times 10^7$ S/m is employed in the full-wave simulator (corresponding to the effective conductivity of the AlSi10Mg alloy employed in SLM). The results for the Q_U factors and volumes of the cavities resonating at $f = f_0$ are presented in Fig. 12. It is interesting to observe that the best Q_U factors are obtained for cavities with $\varphi \approx 105°$, a similar value obtained for the optimal circular torus cavity. On the other hand, the most voluminous cavities are those whose φ value is higher.

The described study is repeated for different fixed values of the radius a_z, between 5 and 10 mm. With all these data, the

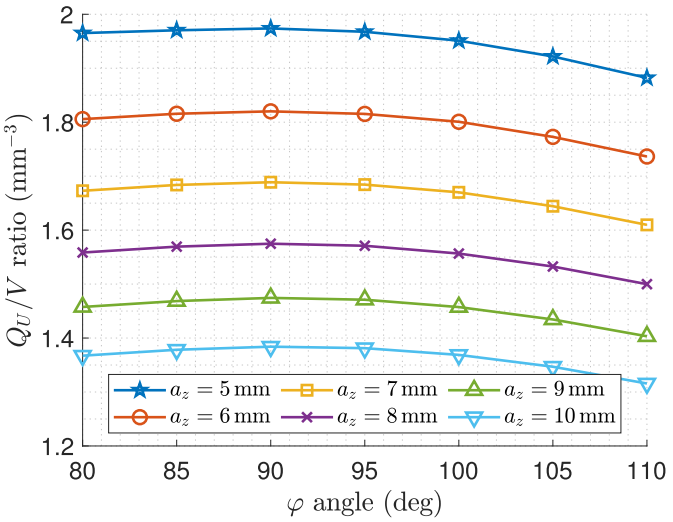

Fig. 13. Q_U/V curves obtained corresponding to several cavities with different φ angles, as a function of AR. Fixed dimensions are $R_{\text{ext}} = 10$ mm and $a_z = 6$ mm. Cavities resonate at a fixed $f_0 = 14.12$ GHz.

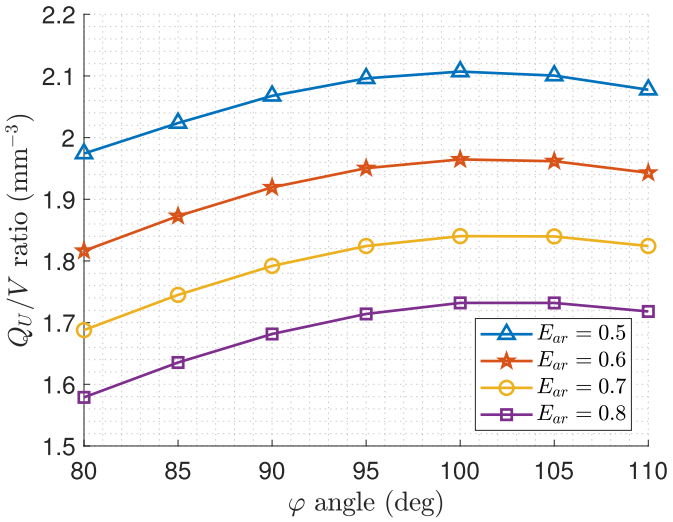

Fig. 14. Results obtained for the figure of merit Q_U/V, corresponding to different values of E_{ar} for a fixed frequency of 14.12 GHz, as a function of the revolution φ angle.

TABLE I

SUMMARY OF THE RESULTS OBTAINED FOR THE OPTIMAL CAVITIES FOUND IN THE STUDY OF THE ELLIPTICAL TORUS CAVITY

a_z	Optimal φ	Q_U/V (mm^{-3})	a_x (mm)	E_{ar}
5 mm	89.64°	1.97	8.95	0.55
6 mm	90.03°	1.82	8.88	0.67
7 mm	90.27°	1.68	8.81	0.80
8 mm	90.66°	1.57	8.71	0.92
9 mm	90.87°	1.47	8.63	1.04
10 mm	91.05°	1.38	8.54	1.17

TABLE II

SUMMARY OF THE RESULTS OBTAINED FOR THE OPTIMAL CAVITIES FOUND IN THE STUDY OF THE ELLIPTICAL TORUS CAVITY, FOR VARIOUS VALUES OF E_{AR}

a_z	Optimal φ	Q_U/V (mm^{-3})	a_x (mm)	E_{ar}
4.09 mm	100.60°	2.11	8.17	0.5
4.85 mm	101.62°	1.96	8.10	0.6
5.62 mm	102.34°	1.84	8.04	0.7
6.41 mm	102.40°	1.73	8.00	0.8

Q_U/V figure of merit is computed, and the resulting curves are presented in Fig. 13. For the sake of clarity, the curves are presented as a function of φ instead of AR. It is interesting to observe that, in this case, the optimal Q_U/V achieved values are located for cavities around $\varphi = 90°$. The exact optimal values for each curve are indicated in Table I.

Although the results obtained from this study may seem contradictory with the optimal cavities obtained for the circular torus cavity, there are a few significant things that need to be remarked. First, in the circular torus study, both radii are fixed to the same value (i.e., the circular torus cross section is similar to the elliptical cavity when $a_x = a_z$ in all cases). By fixing the a_z radius, the modal chart for the obtained cavities is significantly different for each one of the tuned cavities in this study. Looking at the values taken for E_{ar} in each iteration of the study, it is easy to conclude that the spurious behavior of the cavities is substantially different, taking into account the results obtained in Fig. 10.

An alternative possibility is to fix E_{ar} instead of a_z. This study will constrain the studied geometries to those cavities, which show similar spurious behavior. For this purpose, a second study is carried out with the elliptical torus cavity, where a_x is again employed to tune the resonant frequency of each cavity, and a_z is adjusted to the fixed E_{ar} in each analyzed geometry (remember that $E_{\text{ar}} = a_z/a_x$). In this case, R_{ext} is also fixed to 10 mm, a_x is swept between 7.5 and 9.9 mm, φ varies between 80° and 110°, and E_{ar} is fixed for different values between 0.5 and 0.8. The results obtained for the computed Q_U/V values are presented in Fig. 14, as a function of φ. It is interesting to observe that the optimal φ angles are now shifted to values around 100°. The optimal values obtained in this study are collected in Table II. From these values, it can be observed that, as E_{ar} increases and gets closer to $E_{\text{ar}} = 1$ (circular torus cavity), the optimal φ angle increases and approaches to the optimal angle obtained in the circular cavity case, i.e., $\varphi \approx 105°$.

Therefore, the results confirm that in all cases, the optimal cavity is located between $\varphi = 90°$ and $\varphi = 105°$. Depending on the target application requirements, the optimal φ cavity may be one or another.

1) When the spurious performance is important, the best strategy is to fix a_z to push away the spurious resonances. In this cases, lower Q_U values will be achieved, and consequently, higher insertion loss (IL) values are expected in the filter design.
2) When the losses are important, circular torus cavities are preferable. Worse spurious performance is expected, but as an advantage, better Q_U values will be achieved.
3) When resonator size is important, the best trade-off among the electrical performance of the cavity is achieved by fixing E_{ar}, allowing a fine-tune of the Q_U/V figure of merit.

For the filters designed along Section III, an angle of $\varphi = 90°$ is chosen, in order to simplify the geometrical modeling of the structures.

III. Filter Designs With Quart-Torus Resonators

In this section, several designs of in-line bandpass filters using the proposed quart-torus resonator are presented. First, a simple design with four cavities will be performed. With this design, the flexibility in the layout configuration of the proposed cavities is demonstrated, by extending the physical dimensions obtained in the first design to other three possible layouts, with different orientations for the cavities, but using the same dimensions.

Then, the design of a tenth-order in-line bandpass filter is proposed, at Ku-band with a center frequency f_c = 14.12-GHz, 750-MHz bandwidth (BW) [≈5.3% fractional BW (FBW)] and return losses (RLs) higher than 20 dB. This design is manufactured using an SLM technique, and the manufacturing prototype results obtained are discussed in Section IV.

A. Designs With Various Cavity Layouts

One of the interesting properties of the proposed quart-torus cavity lies in its flexibility to optimize the filter layout along the 2-D plane. In order words, it is possible to freely change the quart-torus cavity orientation in an already-designed cavity filter without affecting its electrical performance. In order to illustrate the quart-torus flexibility capabilities, several designs with different cavity layouts are presented in this section. First, a fourth-order in-line filter will be designed following the natural one after each other strategy to place the cavities into the filter. Afterward, taking its dimensions as a baseline, three more designs will be simulated with different cavity layouts, but using the same baseline dimensions, and their electrical performances will be compared.

For the baseline design, the radius a_z is fixed to 6 mm, while the radius a_x is employed to fine-tune the resonant cavities. The couplings between cavity resonators are implemented with typical rectangular irises, and the I/O interface is implemented with a standard WR-62 rectangular waveguide (a = 15.7988 mm and b = 7.8994 mm). The filter dimensions are obtained using a refinement of the classical even–odd frequency analysis technique [20], using the coupling matrix formalism. Its corresponding coupling matrix is synthesized using a classical $N + 2$ technique from general class Chebyshev filter functions [1]. The RL level for this function is fixed to 20 dB, and no prescribed TZs are considered. All elements of this matrix are zero, except for the in-line couplings, yielding

$$\begin{aligned} M_{S1} &= M_{4L} = 1.0352 \\ M_{12} &= M_{34} = 0.9106 \\ M_{23} &= 0.699. \end{aligned} \tag{3}$$

A 2-D schematic of the baseline filter is presented in Fig. 15. Note that the filter geometry is symmetrically distributed from input to output. Therefore, it is only needed to obtain the dimensions for the couplings w_{s1}, w_{12}, and w_{23}, and also the tuning for cavities 1 and 2 (a_{x_1} and a_{x_2}). After the design procedure is applied and a small refinement is carried out to properly equalize the reflection S_{11} response, the final filter dimensions, corresponding to Fig. 15, are as follows:

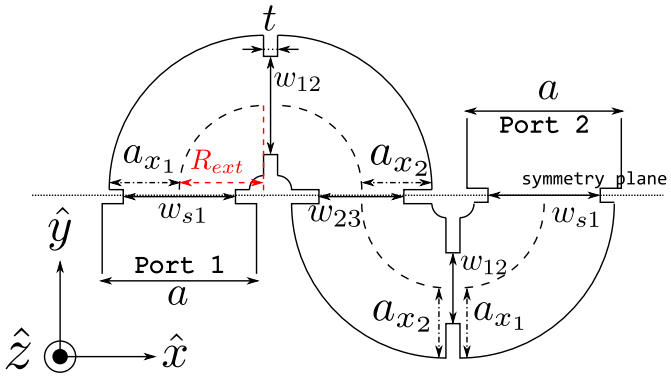

Fig. 15. 2-D schematic of the fourth-order filter. Fixed parameters are as follows: t = 2 mm, a_z = 6 mm, and a = 15.7988 mm. All irises heights are also fixed to b = 7.8994 mm, similar to the I/O rectangular waveguide ports.

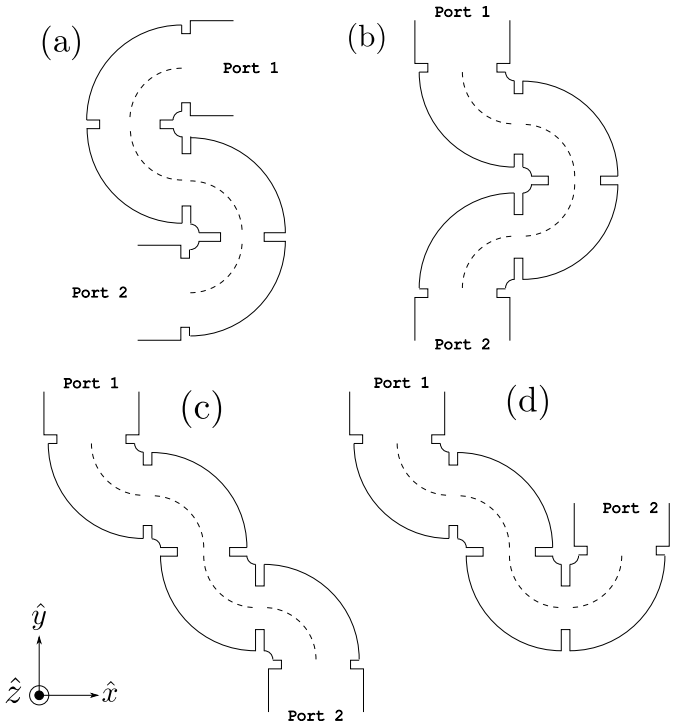

Fig. 16. Various possible schematics of the fourth-order in-line filter, with different cavity layouts along the XY plane. (a) Baseline filter layout. (b) Mirror symmetry filter layout 1. (c) Mirror symmetry filter layout 2. (d) Asymmetrical filter layout.

w_{s1} = 9.352 mm, w_{12} = 7.281 mm, w_{23} = 6.79 mm, a_{x_1} = 7.577 mm, and a_{x_2} = 7.95 mm.

Once the baseline dimensions are obtained, it is possible to generate different layouts for the fourth-order filter using these dimensions, but with different cavity orientations. Since the designed filter only has four cavities, there are four possible variations of this structure along the XY plane, ignoring the symmetrical ones. These layouts are presented in Fig. 16. The baseline filter layout corresponds to Fig. 16(a). Fig. 16(b) and (c) is generated after applying symmetry mirroring to the first half of the filter, whereas Fig. 16(d) is geometrically asymmetrical. However, in all cases, the physical dimensions for the coupling windows and cavity radii are always equal to the baseline dimensions.

Finally, the S-parameter responses of the layouts presented in Fig. 16 are presented in Fig. 17. It can be observed that the

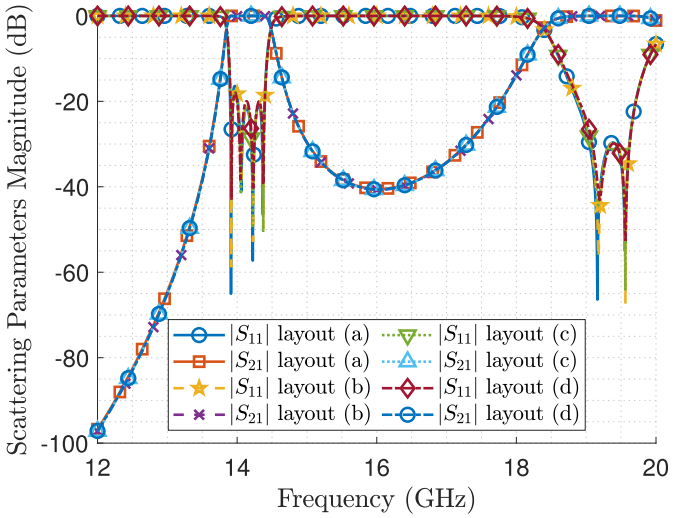

Fig. 17. Scattering parameters of the fourth-order filters designed, using the filter layouts presented in Fig. 16.

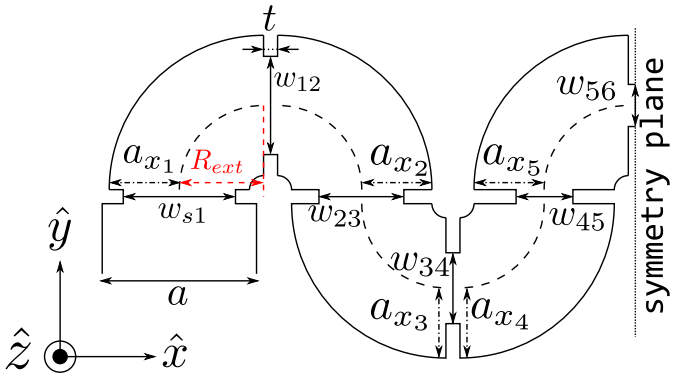

Fig. 18. 2-D schematic of the tenth-order in-line filter. Fixed parameters are as follows: $t = 3$ mm, $a_z = 5$ mm, and $a = 15.798$ mm. The iris height is also fixed to $b = 7.8994$ mm, similar to the I/O waveguide ports.

electrical responses in all cases are identical. The minor disagreements, which are observed in the graph, can be explained due to meshing differences between simulations. The obtained results illustrate the flexibility capabilities of the proposed quart-torus resonators and its potential use in the optimization of communication breadboards in complex systems.

B. Design of a Tenth-Order In-Line Filter

Using the EQT resonator, a tenth-order in-line filter is now designed. In order to avoid spurious resonances from appearing at frequencies close to the passband, the cavity is dimensioned by fixing the radius a_z, and using a_x for the tuning of each cavity. With this strategy, a better control over the spurious resonances is provided, ensuring that the inclusion of screws for tuning or inaccuracies in the manufacturing process do not have a significant impact on the electrical performance of the filter passband.

The couplings between cavity resonators are implemented with typical rectangular irises, and the I/O interface is implemented with a standard WR-62 waveguide ($a = 15.7988$ mm and $b = 7.8994$ mm). The filter dimensions are obtained using a refinement of the classical even–odd frequency analysis technique [20], using the coupling matrix formalism. Its corresponding coupling matrix is synthesized using a classical $N + 2$ technique from general class Chebyshev filter functions [1]. All elements of this matrix are zero, except for the in-line couplings, yielding

$$\begin{aligned} M_{S1} &= M_{10-L} = 0.985, \quad M_{12} = M_{9-10} = 0.813 \\ M_{23} &= M_{89} = 0.584, \quad M_{34} = M_{78} = 0.544 \\ M_{45} &= M_{67} = 0.532, \quad M_{56} = 0.529. \end{aligned} \tag{4}$$

A 2-D schematic of the designed filter is presented in Fig. 18, where the main physical dimensions of the structure are illustrated. For the EQT resonators, a_x is tuned to adjust the resonant frequency of each cavity, while a_z is fixed to 5 mm. The coupling rectangular windows are adjusted using the width w_{ij}, while the thickness is set to $t = 3$ mm. The height of the windows is equal to the I/O ports height ($b = 7.8994$ mm). Since the filter geometry is symmetrical, only one half of the structure is shown in Fig. 18.

Due to typical accuracy achieved in AM techniques [21], the filter needs tuning screws. In view of the expected dimensional tolerances, provided by the manufacturer, around ± 100 μm, significant response deviations may appear due to numerical errors during the printing process. In order to account for these possible deviations, a sensitivity analysis has been conducted over a tenth-order filter with EQT cavities without considering tuning screws. The geometrical parameters, which have been included into the analysis, correspond to the variables employed during the design stage (i.e., the rectangular window widths and the elliptical semiaxis a_x). The electrical responses after several simulations have been run are presented in Fig. 19. For the sake of clarity, only the reflection S_{11} parameter is included in the graph corresponding to each iteration of the sensitivity analysis. It can be easily observed that the S-parameters in many cases are very far from the baseline response, indicating that a severe degradation of the performance is obtained. After the initial filter dimensions are obtained, the tuning screws are incorporated into the model. This requires a readjustment of the filter physical dimensions in order to account for the frequency and coupling deviations introduced by these screws. The filter is finally tuned for a geometry with all tuning screws introduced halfway of its total penetration. The final 3-D model considering M2 tuning screws (modeled as circular cylinders) is shown in Fig. 20.

The resulting dimensions after the final refinement employing the complete model considering tuning screws are collected in Table III. The corresponding S-parameters response is presented in Fig. 21. The final optimized response obtained in the simulation is good in terms of RL, BW, and center frequency. The small deviations observed from the ideal specifications can be corrected in the post-manufacturing stage via the fine-tuning process using the M2 screws incorporated into the structure. In this figure, it can also be observed that the first spurious resonances are located at ≈ 17.5 GHz. These transmission peaks are caused by the resonant TM mode, which is excited due to the introduction of cylinders to model the tuning screws in the Ansys HFSS model. These spurious resonances would be too close to the passband if a circular

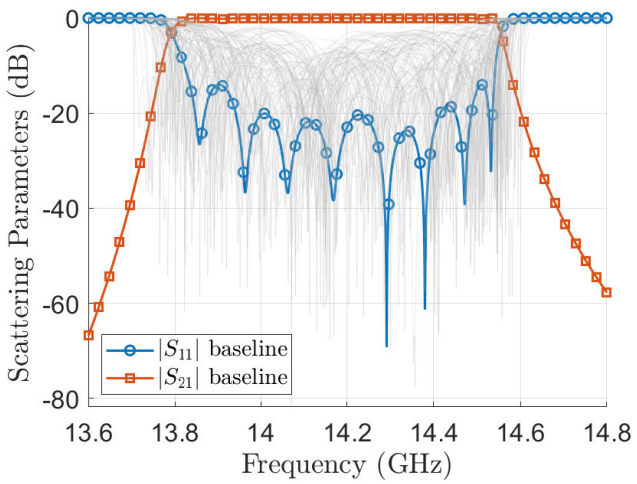

Fig. 19. Results for the sensitivity analysis with random errors applied of ± 100 μm. $|S_{11}|$ curves are only presented for the batch of simulations in the sensitivity study.

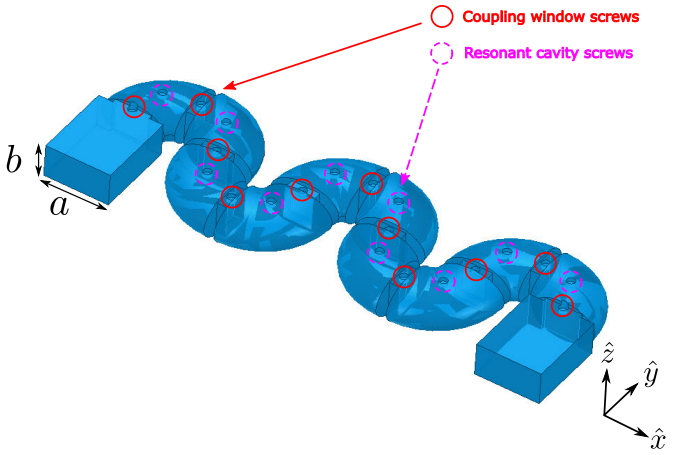

Fig. 20. CAD 3-D model of the manufactured filter, showing the position of the M2 tuning screws modeled as circular cylinders. I/O ports are standard WR-62. The printing direction in the 3-D printer bed corresponds to a 45° rotated piece with respect to the $\hat{x}$- and $\hat{y}$-axes.

TABLE III

DIMENSIONS (IN MM) FOR THE TENTH-ORDER IN-LINE ELLIPTIC QUART-TORUS RESONATOR FILTER, CORRESPONDING TO FIG. 18. FIXED DIMENSIONS ARE AS FOLLOWS: $t = 3$ MM, $a_x = 5$ MM, AND $a = 15.978$ MM. ALL IRISES HEIGHT ARE ALSO FIXED TO $b = 7.8994$ MM

w_{s1}	8.866	w_{45}	6.852	a_{x_3}	8.236
w_{12}	7.731	w_{56}	6.831	a_{x_4}	8.29
w_{23}	7.107	a_{x_1}	7.73	a_{x_5}	8.314
w_{34}	6.915	a_{x_2}	8.041		

quart-torus cavity is chosen instead of an elliptical one. This result shows a good agreement with the eigenmode simulations presented in Fig. 10, as the spurious resonances (mode 1) appear approximately 3.5 GHz higher in frequency than the operating resonance (mode 2).

IV. MANUFACTURING RESULTS AND DISCUSSION

The designed structure has been manufactured from a single piece using a direct metal laser sintering (DMLS) machine (an EOS M280), using an aluminum alloy typically employed in 3-D printing (AlSi10Mg) (see Fig. 22). No post-manufacturing heat treatment or polishing is applied to the prototype. The expected surface roughness is $\approx$ 15 μm and dimensional tolerances of ± 100 μm. It can be observed that two WR-62 standard flanges are incorporated, in order to allow the filter connection to the waveguide measurement kit. Only the faces of the flanges connecting to the measurement kit are mechanically polished.

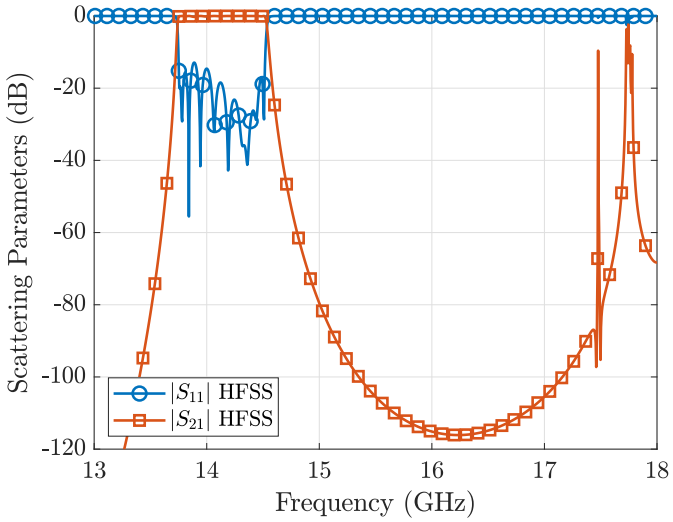

Fig. 21. Simulated scattering parameters of the designed tenth-order in-line filter shown in Fig. 20. The new elliptical cross-sectional cavity shows a large SFR, with the first resonance appearing at 17.5 GHz.

As it is manufactured as a single part, no assembly screws are needed. The holes corresponding to the positions of the tuning screws are not 3-D printed. Instead, they are milled into the structure after finishing the 3-D printing process. The reason for this is to avoid inaccuracies due to misalignment of the screws. The inner surface of the structure is not treated in any way. Therefore, the high roughness of the surfaces is expected to translate into a drop in Q_U. Only the external face of the WR-62 flanges is mechanically polished, to ensure a good current continuity between the filter I/O ports and the waveguide flanges of the measurement kit.

In Fig. 23, a comparison of the response recovered after fine-tuning the structure and the ideal response from the Ansys HFSS simulation is presented. The filter is simulated using an ideal flat surface model for the aluminum aluminum-alloy waveguide walls (using the worst conductivity value provided by the manufacturer, which is σ_{AlSi10Mg}) and brass (with $\sigma_{\text{Br}} = 1.5 \times 10^7$ S/m) for the included tuning screws. The results show that a good agreement has been achieved between the measured and simulated filter responses. On the one hand, the RL level is tuned to its best possible value, obtaining RL = 22.5 dB. On the other hand, the passband central frequency is slightly shifted to $f_c(\text{meas}) = 14.08$ GHz.

A very important difference is found in the IL levels between the measured filter and the lossy simulated structure. For the 3-D printed prototype, a level of $\text{IL}_m = 1.953$ dB is obtained, while the simulated loss level is $\text{IL}_s = 0.4285$ dB. Since the obtained IL level is significantly higher than the values typically obtained in waveguide filters, a more in-depth

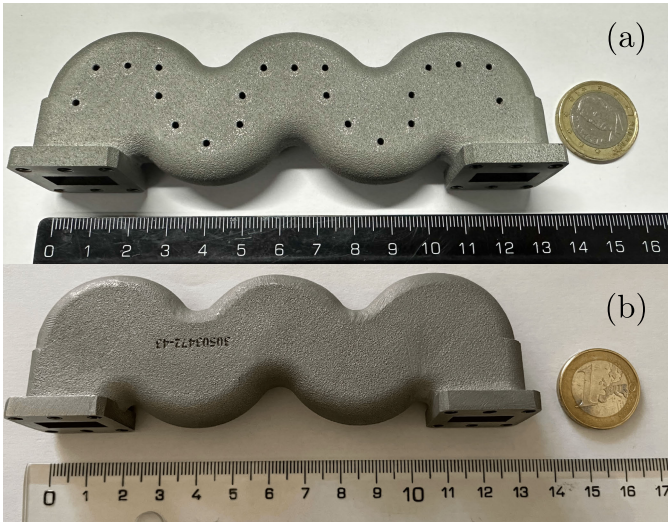

Fig. 22. Photograph showing the final manufactured prototype, compared with a measure ruler and an euro coin. (a) Top view of the prototype, illustrating the threads for the tuning screws according to Fig. 20. (b) Bottom view of the prototype.

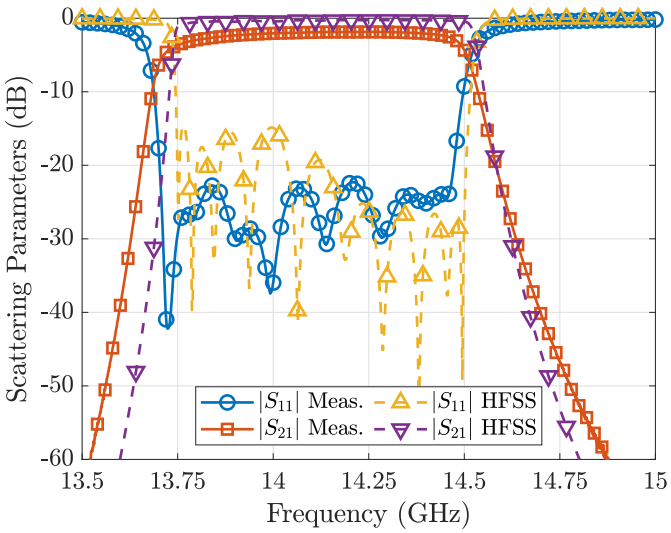

Fig. 23. Measured S-parameter response compared with Ansys HFSS lossy simulation, with AlSi10Mg walls.

study is performed to evaluate the electrical performance of the device.

First, the effective Q_U factor of the manufactured cavity can be evaluated. For synchronously tuned in-line filters, an empirical relation is available to estimate the Q_U factor as a function of the Nth-order filter center frequency f_0, BW, ideal low-pass prototype elements g_r, and IL [22], as follows:

$$Q_U = \frac{4.343\, f_0}{\mathrm{BW} \cdot \mathrm{IL}} \sum_{r=1}^{N} g_r. \tag{5}$$

This expression can be applied to both measured and simulated responses to obtain the estimated Q_U values. For the measured structure, a $Q_{U_m} = 767.19$ is obtained, which is an 84% of quality factor reduction in relation with the simulated value $Q_{U_s} = 4470.9$. Other SLM waveguide filters, such as the structures reported in [13], show a Q_U reduction above 50% due to the 3-D printing process, and associated surface roughness. However, it is known that a proper post-manufactured surface treatment, such as chemical polishing and silver plating, is effective in retrieving most of the theoretical Q_U.

TABLE IV
COMPARATIVE DIMENSIONS BETWEEN THE DESIGNED EQT FILTER AND A SIMILAR FREQUENCY SPECIFICATIONS DESIGN USING ALL-INDUCTIVE RECTANGULAR-WAVEGUIDE TECHNOLOGY (WR)

	Width (mm)	Height (mm)	Length (mm)	Volume (mm^3)
WR	15.799	7.8994	178.75	21427.97
EQT	38.6	10	121.1988	25072.49
Diff	244.32%	126.6%	67.8%	117

However, the Q_U reduction is more than the mentioned 50%, which indicates that the surface roughness is not the only root cause for the filter IL degradation. In addition to the analysis to compute the effective Q_U, it is also possible to obtain the effective conductivity of the resulting prototype. To perform this analysis, several simulations have been carried out with the geometry of the manufactured prototype, where the conductivity of the metallic walls was adjusted until a simulated value for the IL obtained has a similar value to the IL measured with the vector network analyzer. As a result, an effective conductivity of $\sigma_{\text{test}} = 2.85 \times 10^6$ S/m was obtained. It is observed that this value is significantly far from the expected conductivity value of the alloy, around $\sigma = 1.7 \times 10^7$ S/m. Clearly, there exists a significant degradation in the electrical performance of the filter. However, the resulting conductivity values from the conducted study are to be expected. In [23], an experimental study was carried out to determine the typical electrical conductivity of the metallic alloy employed with the EOS M280 tool, by printing a rectangular waveguide section measured between 8 and 11.25 GHz. The authors report a measured σ ranging between 5×10^5 and 1×10^6 S/m. Since these values are very similar to σ_{test}, which is measured at a higher frequency, it can be concluded that the manufactured sample is in accordance with the typical performance of the 3-D-printer machine.

In the authors' opinion, there are various causes for the obtained prototype degradation: inaccuracies of the 3-D printing procedure, significant surface roughness, and a large contribution of the brass screws to the IL. All of these issues lead to a poor performance of the prototype in terms of losses, even though the frequency specs of the filter have been properly fulfilled. In addition, the typical conductivities achieved for an X-band waveguide, as discussed in [23], indicate that the loss performance of the prototype is to be expected with a manufactured piece using the EOS M280 tool. A mechanical polishing would significantly increase the effective conductivity of the printed piece, as discussed in [23]. However, in this case, due to the complex meandered cavity layout, it is impossible to properly access the internal walls of the filter. A mechanical polishing or a silver coating may also help increasing the poor resulting conductivity, even though these posttreatment techniques cannot be applied in a uniform way, due to the geometrical complexity of the internal walls of the filter, and it could become impossible to recover

TABLE V

COMPARISON TABLE OF THE PROTOTYPE FILTER WITH SEVERAL ADDITIVE MANUFACTURED FILTERS. SIMULATED AND MEASURED Q_U FACTORS ARE ESTIMATED USING (5), FROM THE DATA GIVEN IN THE PAPERS OF IL, f_c, AND BW. (*): VALUE DIRECTLY GIVEN IN THIS ARTICLE FOR A SIMULATED EQUIVALENT RECTANGULAR CAVITY. (**): VALUE DIRECTLY GIVEN IN THIS ARTICLE BY MEANS OF GROUP DELAY IL MEASUREMENT. λ_c IS THE VACUUM WAVELENGTH CALCULATED AT THE FILTER CENTRAL FREQUENCY. REF: REFERENCE. T.W.: THIS WORK. f_c: CENTRAL FREQUENCY. FBW: FRACTIONAL BANDWIDTH. SLM: SELECTIVE LASER MELTING. SLA: STEREOLITHOGRAPHY. N/G: NOT GIVEN

Ref.	Resonator technology	f_c	Res. Elec. Size	Q_U (sim.)	Q_U (meas.)	Material	Manuf.
[14]	Depressed super ellipsoid	12.87	N/G	4400*	4300**	Silver coat.	SLM + Plating
[17]	Squeezed spherical resonator	10	$0.83\lambda_c \times 0.56\lambda_c \times 0.83\lambda_c$	4566	4057	AlSi10Mg	SLM + Chem. Polish
[24]	Spherical cavity resonators	10	$0.33\lambda_c \times 0.33\lambda_c \times 0.33\lambda_c$	7834.53	5271.83	Copper	SLA + Plating
[26]	Dual-mode spherical cavity	10	$0.82\lambda_c \times 0.82\lambda_c \times 0.82\lambda_c$	4409.28	1945.27	Copper	SLA + Plating
[27]	Dual-mode ellipsoidal cavity	10	$0.38\lambda_c \times 0.42\lambda_c \times 0.41\lambda_c$	N/G	341.68	Silver Ink	SLA + Coating
[28]	Hemispherical cavity	32	$0.8\lambda_c \times 0.41\lambda_c \times 0.8\lambda_c$	N/G	313.35	Silver coat.	SLA + Heat treat. + Plating
T.W.	Elliptical quart-torus cavity	14.12	$0.75\lambda_c \times 0.75\lambda_c \times 0.47\lambda_c$	4470.9	767.19	AlSi10Mg	SLM (Untreated)

the frequency response and BW of the prototype after its application. Therefore, a new manufacturing with a different printer may be required to reduce excessive loss resulting from this prototype.

If we compare the designed quart-torus filter with a similar one designed using rectangular cavities (WR-62) coupled with inductive irises (rectangular windows), the footprint redistribution becomes evident. In Table IV, a collection of the most relevant dimensions of each filter is presented. The dimensions given as width, height, and length are taken using the maximum distance in each dimensions (i.e., the bounding box for each filter), while the volume is directly computed from the 3-D computer-aided design (CAD) model, and not using the volume of the bounding box. As expected, the bending applied to the structure achieves a length reduction of 67% as compared with the typical rectangular waveguide filter. This result clearly shows the great flexibility in footprint distribution that can be obtained by using the new cavity proposed in this article.

Note that the filters used in the above comparison are always operating as single-mode resonators. This is because the dual-mode capabilities of the quart-torus resonator have not been explored yet, and therefore, the comparison between dual-mode filters with various technologies and single-mode quart-torus structures is not fair. Also, foldings in the standard waveguide technologies have not been considered for a similar reason.

For the sake of completeness, an additional comparison between the proposed structures and other filters from the technical literature is presented in Table V. For a fair comparison in terms of size, the dimensions of each resonator technology are compared in terms of λ_c, where λ_c is the wavelength computed in a free space, at the resonator central frequency f_c. It can be observed that the size performance among all the resonators compared is similar, except for the spherical cavity resonators used in [24], where a higher order mode of the cavity was employed.

The Q_U values given in the table are computed from the IL, central frequency, and BW values given in the referenced papers for the manufactured prototypes, using (5). This comparison gives an estimated orientation of the performance to be expected with each resonator technology employed. At this point, it is important to remark that the achievable Q_U is dependent of the lossy material of the prototype, as well as the resonant frequency of the resonator. It can also be observed that performances between simulated and measured Q_U are not similar in all cases. This illustrates that, depending on the filter geometrical complexity and the 3-D-printing tool employed, the loss performance of the resulting prototype can be significantly degraded. The best Q_U performance is achieved, in general, for SLA-coated parts, which seems to lead to better effective conductivities for the resulting pieces, although its use is not recommended in space applications due to thermal issues [25], in contrast with the most well-accepted SLM printing. In general, it can be stated that the proposed quart-torus filter is an interesting solution to achieve a reasonable trade-off among size, spurious performance, and losses in contrast with other novel filter structures proposed in the literature due to the emerging of AM techniques.

V. CONCLUSION

In this contribution, a novel cavity geometry based on a modification of the circular cylindrical waveguide cavity is presented. By applying a bending to the longitudinal axis, a quart-torus resonator is proposed, which shows interesting electrical performances. One important advantage is the geometrical flexibility offered by the new cavity, since it allows to implement similar filter topologies with different physical layouts. The original structure based on a circular geometry was modified into an elliptical shape to separate the fundamental resonance from other spurious modes. A tenth-order filter is designed and manufactured from a single block using AM techniques, to demonstrate the feasibility of the proposed EQT cavity in the design of practical microwave filters. Measured results show good agreement with respect to target specifications, and within typical limitations of the current state of the art of AM processes. The manufactured prototype shows a reduction in length of 67% with respect to a similar filter using classical rectangular waveguide technology. This work shows that the flexibility introduced by AM techniques will certainly allow in the coming years to further optimize traditional filter designs.

REFERENCES

[1] R. J. Cameron, C. M. Kudsia, and R. R. Mansour, *Microwave Filters for Communication Systems: Fundamentals, Design and Applications*, 2nd ed. Hoboken, NJ, USA: Wiley, 2018.

[2] G. Matthaei, L. Young, and E. Yones, *Microwave Filters, Impedance Matching Networks, and Coupling Structures*. Norwood, MA, USA: Artech House, 1980.

[3] O. A. Peverini et al., "Additive manufacturing of Ku/K-band waveguide filters: A comparative analysis among selective-laser melting and stereo-lithography," *IET Microw., Antennas Propag.*, vol. 11, no. 14, pp. 1936–1942, Nov. 2017.

[4] T. Horn et al., "Additively manufactured WR-10 copper waveguide," in *Proc. IEEE Int. Vac. Electron. Conf. (IVEC)*, Apr. 2018, pp. 409–410.

[5] S. Verploegh, M. Coffey, E. Grossman, and Z. Popovic, "Properties of 50–110-GHz waveguide components fabricated by metal additive manufacturing," *IEEE Trans. Microw. Theory Techn.*, vol. 65, no. 12, pp. 5144–5153, Dec. 2017.

[6] D. C. Lugo, R. A. Ramirez, J. Castro, J. Wang, and T. M. Weller, "Ku-band additive manufactured multilayer dielectric rod waveguide," in *Proc. IEEE 18th Wireless Microw. Technol. Conf. (WAMICON)*, Apr. 2017, pp. 1–3.

[7] B. Zhang and H. Zirath, "Metallic 3-D printed rectangular waveguides for millimeter-wave applications," *IEEE Trans. Compon., Packag., Manuf. Technol.*, vol. 6, no. 5, pp. 796–804, May 2016.

[8] B. Zhang et al., "Metallic 3-D printed antennas for millimeter- and submillimeter wave applications," *IEEE Trans. Terahertz Sci. Technol.*, vol. 6, no. 4, pp. 592–600, Jul. 2016.

[9] G. McKerricher, A. Nafe, and A. Shamim, "Lightweight 3D printed microwave waveguides and waveguide slot antenna," in *Proc. IEEE Int. Symp. Antennas Propag. USNC/URSI Nat. Radio Sci. Meeting*, Jul. 2015, pp. 1322–1323.

[10] G. J. Schiller, "Additive manufacturing for aerospace," in *Proc. IEEE Aerosp. Conf.*, Mar. 2015, pp. 1–8.

[11] C. W. J. Lim, K. Q. Le, Q. Lu, and C. H. Wong, "An overview of 3-D printing in manufacturing, aerospace, and automotive industries," *IEEE Potentials*, vol. 35, no. 4, pp. 18–22, Jul. 2016.

[12] A. Maamoun, Y. Xue, M. Elbestawi, and S. Veldhuis, "Effect of selective laser melting process parameters on the quality of Al alloy parts: Powder characterization, density, surface roughness, and dimensional accuracy," *Materials*, vol. 11, no. 12, p. 2343, Nov. 2018.

[13] J. A. Lorente, M. M. Mendoza, A. Z. Petersson, L. Pambaguian, A. A. Melcon, and C. Ernst, "Single part microwave filters made from selective laser melting," in *Proc. Eur. Microw. Conf. (EuMC)*, Sep. 2009, pp. 1421–1424.

[14] P. Booth and E. V. Lluch, "Enhancing the performance of waveguide filters using additive manufacturing," *Proc. IEEE*, vol. 105, no. 4, pp. 613–619, Apr. 2017.

[15] F. Teberio et al., "Meandered corrugated waveguide low-pass filter," in *IEEE MTT-S Int. Microw. Symp. Dig.*, Sep. 2017, pp. 1–3.

[16] F. Teberio et al., "Rectangular waveguide filters with meandered topology," *IEEE Trans. Microw. Theory Techn.*, vol. 66, no. 8, pp. 3632–3643, Aug. 2018.

[17] C. Guo et al., "Shaping and slotting high-Q spherical resonators for suppression of higher order modes," in *IEEE MTT-S Int. Microw. Symp. Dig.*, Jun. 2019, pp. 1205–1208.

[18] J. Zhang, B. Song, Q. Wei, D. Bourell, and Y. Shi, "A review of selective laser melting of aluminum alloys: Processing, microstructure, property and developing trends," *J. Mater. Sci. Technol.*, vol. 35, no. 2, pp. 270–284, Feb. 2019.

[19] (2020). *Ansys Electronics Desktop, Release R1*. ANSYS. Canonsburg, PA, USA. [Online]. Available: https://ansys.com

[20] A. Pons-Abenza, A. Alvarez-Melcon, F. D. Quesada-Pereira, and L. Arche-Andradas, "Frequency correction design technique for additive manufactured cavity filters," in *Proc. 48th Eur. Microw. Conf. (EuMC)*, Sep. 2018, pp. 288–291.

[21] J. Kruth, P. Mercelis, J. Van Vaerenbergh, L. Froyen, and M. Rombouts, "Binding mechanisms in selective laser sintering and selective laser melting," *Rapid Prototyping J.*, vol. 11, no. 1, pp. 26–36, Feb. 2005.

[22] I. C. Hunter, L. Billonet, B. Jarry, and P. Guillon, "Microwave filters-applications and technology," *IEEE Trans. Microw. Theory Techn.*, vol. 50, no. 3, pp. 794–805, Mar. 2002.

[23] M. D. Benge, R. C. Huck, and H. H. Sigmarsson, "X-band performance of three-dimensional, selectively laser sintered waveguides," in *Proc. IEEE Antennas Propag. Soc. Int. Symp. (APSURSI)*, Jul. 2014, pp. 13–14.

[24] C. Guo, X. Shang, M. J. Lancaster, and J. Xu, "A 3-D printed lightweight X-band waveguide filter based on spherical resonators," *IEEE Microw. Wireless Compon. Lett.*, vol. 25, no. 7, pp. 442–444, Jul. 2015.

[25] P. Vaitukaitis, K. Nai, J. Rao, M. S. Bakr, and J. Hong, "Technological investigation of metal 3-D printed microwave cavity filters based on different topologies and materials," *IEEE Trans. Compon., Packag., Manuf. Technol.*, vol. 12, no. 12, pp. 2027–2037, Dec. 2022.

[26] C. Guo, X. Shang, J. Li, F. Zhang, M. J. Lancaster, and J. Xu, "A lightweight 3-D printed X-band bandpass filter based on spherical dual-mode resonators," *IEEE Microw. Wireless Compon. Lett.*, vol. 26, no. 8, pp. 568–570, 2016.

[27] E. López-Oliver and C. Tomassoni, "3-D-Printed dual-mode filter using an ellipsoidal cavity with asymmetric responses," *IEEE Microw. Wireless Compon. Lett.*, vol. 31, no. 6, pp. 670–673, Jun. 2021.

[28] J. Li, C. Guo, L. Mao, J. Xiang, G.-L. Huang, and T. Yuan, "Monolithically 3-D printed hemispherical resonator waveguide filters with improved out-of-band rejections," *IEEE Access*, vol. 6, pp. 57030–57048, 2018.

Alejandro Pons-Abenza was born in Murcia, Spain, in 1990. He received the master's degree in telecommunications systems engineering and the Ph.D. degree in information and communications technology from the Universidad Politécnica de Cartagena (UPCT), Cartagena, Spain, in 2014 and 2019, respectively.

In 2014, he joined the Department of Information and Communication Technologies, UPCT, as a Research Student. In 2016, he began a research project with the objective of developing his Ph.D. thesis, fruit of a collaboration between UPCT and Thales Alenia Space, Tres Cantos, Spain, for the design and development of novel microwave filter structures using additive manufacturing techniques for space applications. In 2020, he joined the Department of Computer Science, Universidad de Alcalá, Alcalá de Henares, Spain, as a Post-Doctoral Researcher in computational electromagnetism. In 2022, he joined the Department of Electric, Electronic and Communications Engineering, Universidad Pública de Navarra, Pamplona, Spain, as a Post-Doctoral Researcher under a Margarita Salas Grant, where he is currently developing his professional activity. His current research interests include the analysis and design of microwave devices employing additive manufacturing, and synthesis techniques for the design of microwave filters in various technologies.

Alejandro Álvarez-Melcón (Senior Member, IEEE) was born in Madrid, Spain, in 1965. He received the master's degree in telecommunications engineering from the Technical University of Madrid (UPM), Madrid, in 1991, and the Ph.D. degree in electrical engineering from the Swiss Federal Institute of Technology, Lausanne, Switzerland, in 1998.

In 1988, he joined the Signal, Systems and Radiocommunications Department, UPM, as a Research Student, where he was involved in the design, testing, and measurement of broadband spiral antennas for electromagnetic measurements support (EMS) equipment. From 1991 to 1993, he was with the Radio Frequency Systems Division, European Space Agency (ESA/ESTEC), Noordwijk, The Netherlands, where he was involved in the development of analytical and numerical tools for the study of waveguide discontinuities, planar transmission lines, and microwave filters. From 1993 to 1995, he was with the Space Division, Industry Alcatel Espacio, Madrid, and also with the ESA, where he collaborated in several ESA/European Space Research and Technology Centre (ESTEC) contracts. From 1995 to 1999, he was with the Swiss Federal Institute of Technology, École Polytechnique Fédérale de Lausanne (EPFL), Lausanne, where he was involved in the field of microstrip antennas and printed circuits for space applications. He was an Invited Professor with the Polytechnique Montréal, Montreal, QC, Canada from July 1, 2010 to September 30, 2010; and a Visiting Professor with the University of California at Davis, Davis, CA, USA, from October 2, 2017 to September 27, 2018. In 2000, he joined the Universidad Politécnica de Cartagena, Cartagena, Spain, where he is currently developing his teaching and research activities.

Dr. Álvarez-Melcón was a recipient of the *Journée Internationales de Nice Sur les Antennes* (JINA) Best Paper Award for the best contribution to the JINA'98 International Symposium on Antennas and the *Colegio Oficial de Ingenieros de Telecomunicación* (COIT/AEIT) Award to the best Ph.D. dissertation in basic information and communication technologies.

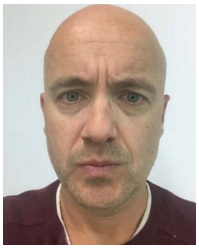

Fernando Daniel Quesada-Pereira (Member, IEEE) was born in Murcia, Spain, in 1974. He received the master's degree in telecommunications engineering from the Technical University of Valencia (UPV), Valencia, Spain, in 2000, and the Ph.D. degree from the Universidad Politécnica de Cartagena (UPCT), Cartagena, Spain, in 2007.

In 1999, he joined the Radiocommunications Department, UPV, as a Research Assistant, where he was involved in the development of numerical methods for the analysis of anechoic chambers and tag antennas. In 2001, he joined the Department of Information and Communication Technologies, UPCT, as a Research Assistant, and then as an Assistant Professor. In 2005, he was a Visiting Scientist with the University of Pavia, Pavia, Italy. In 2009, he was an Invited Researcher with UPV. In 2011, he became an Associate Professor with UPCT. His current research interests include integral equation numerical methods for the analysis of antennas and microwave devices, along with microwave filters design and applications.

Antonio Romera-Pérez was born in Lorca, Spain, in 1989. He received the master's degree in telecommunications systems engineering and the Ph.D. degree in information and communications technology from the Universidad Politécnica de Cartagena (UPCT), Cartagena, Spain, in 2014 and 2020, respectively.

In 2014, he joined the Department of Information and Communication Technologies, UPCT, as a Research Student. In 2016, he began a research project with the objective of developing his Ph.D. thesis, fruit of a collaboration between UPCT and Thales Alenia Space, Tres Cantos, Spain, for the design and development of tunable microwave filters in planar and nonplanar technologies for space applications. He continued as an Associate Researcher at UPCT until he joined FOSSA Systems, Madrid, Spain, as an RF Equipment Design Engineer in March 2022. In 2023, he joined Safran, Granada, Spain, as a Research and Development Engineer, where he currently develops his professional activity. His current scientific interests include the design of microwave circuits and RF equipment for space and ground applications.

Lara Arche-Andradas was born in Madrid, Spain, in 1984. She received the master's degree in telecommunications engineering from the Universidad Politécnica de Madrid (UPM), Madrid, in 2010.

In 2008, she started a fellowship at Thales Alenia Space, Tres Cantos Spain, the results of which she presented as her final dissertation. After that, she joined the company as a Passive RF Engineer with the Research and Development Department, where she participated in research and development projects related to the improvement of input filters for input multiplexers and bandpass filters based on ceramic resonator technology. Subsequently, from 2011 to 2016, she was technically responsible for commercial projects designing input multiplexers and low-pass and bandpass filters for commercial telecommunication satellites in the L, S, C, X, Ku, and Ka frequency bands. From 2016 to 2018, she returned to activities more related to research and innovation, participating in European Space Agency (ESA), Noordwijk, The Netherlands, and internal company projects with high innovative load, employing, for example, MEMS technologies or designing resonator filters for bands above 30 GHz, and being an industrial tutor of Ph.D. candidates in disruptive technologies. As of 2019, she is the Innovation Manager of Thales Alenia Space, where she collaborates in the creation and development of innovative product and business solutions for the space market. She establishes collaborations with universities and startups; supervises degree, master, and Ph.D. projects; and participates in state-of-the-art technological research. She was also a Pioneer within her company in bringing agile methodologies to the hardware environment, is a Business Mentor certified by Madri + d, Madrid, and is widely familiar with the Lean Startup methodology having been part of an internal startup of international character within Thales Alenia Space.

Prof. Arche-Andradas received the company's Innovation Award.